Size-broadening anisotropy in whole powder pattern fitting. Application to zinc oxide and interpretation of the apparent crystallites in terms of physical models
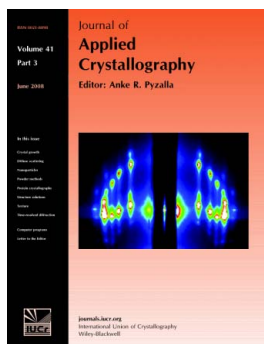
N. C. Popa and D. Balzar

Many research topics in condensed matter research, materials science and the life sciences make use of crystallographic methods to study crystalline and non-crystalline matter with neutrons, X-rays and electrons. Articles published in the *Journal of Applied Crystallography* focus on these methods and their use in identifying structural and diffusion-controlled phase transformations, structure–property relationships, structural changes of defects, interfaces and surfaces, *etc.* Developments of instrumentation and crystallographic apparatus, theory and interpretation, numerical analysis and other related subjects are also covered. The journal is the primary place where crystallographic computer program information is published.

Crystallography Journals Online is available from journals.iucr.org

Size-broadening anisotropy in whole powder pattern fitting. Application to zinc oxide and interpretation of the apparent crystallites in terms of physical models

N. C. Popa[a,b] and D. Balzar[c]*

[a]Frank Laboratory of Neutron Physics, Joint Institute for Nuclear Research, 141980 Dubna, Russian Federation, [b]Institute of Materials Physics, PO Box MG-7, Bucharest, Romania, and [c]Department of Physics and Astronomy, University of Denver, CO 80208, USA. Correspondence e-mail: balzar@du.edu

A new anisotropic size-broadening model based on a spherical-harmonics representation allowing determination of both volume- and area-averaged apparent crystallites and convenient for implementation into Rietveld programs is described. The model effectiveness is demonstrated on a ZnO powder pattern exhibiting strongly anisotropic size broadening and pronounced super-Lorentzian peak shapes. Moreover, it is shown how the apparent crystallites can be interpreted in terms of physical models by using ellipsoidal and cylindrical crystallites with lognormal size distributions. This interpretation is critically assessed and it is argued that both simplified physical models and *a priori* complementary information (obtained by transmission electron microscopy, for instance) are often needed to avoid unstable and non-unique solutions.

1. Introduction

It was recognized early on (Scherrer, 1918) that the small size of crystallites leads to broadening of line profiles in powder diffraction patterns. Line-broadening analysis became more sophisticated with the advent of Fourier (Bertaut, 1949; Warren & Averbach, 1950) and variance (Wilson, 1962) methods. As much as the anisotropy of size broadening was treated in several early theoretical papers (Wilson, 1969; Langford & Louër, 1982; Vargas *et al.*, 1983) and applications (Louër *et al.*, 1972, 1983; Langford *et al.*, 1993), the modeling of anisotropy was particularly advanced with the introduction of size-broadening models in Rietveld refinement programs.

Two models of size-broadening anisotropy are currently used in Rietveld programs. A model of infinite plates and needles, originally proposed by Greaves (1985), is implemented in *GSAS* (Larson & Von Dreele, 1986). The crystal rotation axis is normal to the plate or parallel to the needle axis. The breadth of the diffraction peak then depends only on the angle between this axis and the scattering vector. There is no broadening effect in the plane of the plate or along the needle axis. No size distribution is considered; consequently the model has only one refinable parameter, the plate thickness or the needle diameter.

The second model of size-broadening anisotropy implemented in Rietveld codes is the phenomenological model of spherical harmonics proposed by Popa (1998). It was implemented in the Rietveld program *MAUD* (Lutterotti, 1997)

and applied by Lutterotti *et al.* (1999) to determine the apparent anisotropic crystallite of chromium oxide from the Rietveld refinement of an X-ray diffraction pattern. Later the model was implemented in *FULLPROF* by Rodriguez-Carvajal (2001). Using *FULLPROF*, Casas-Cabanas *et al.* (2005) have recently interpreted the anisotropic line broadening in the patterns of four samples of nickel hydroxide as an alternative solution to anisotropic broadening caused by stacking faults.

The model of spherical harmonics proposed by Popa (1998) is based on the observation that the volume-averaged column length in the Scherrer (1918) formula, $D_V(\mathbf{h})$, is invariant to the Laue group operations, and therefore can be expanded in a series of symmetrized spherical harmonics of polar and azimuthal angles of $\mathbf{h}$, the unit vector along the reciprocal lattice vector $\mathbf{H}$. The spherical harmonics coefficients are refined in whole pattern fitting. The size-broadened peak shape was considered Lorentzian.

The spherical harmonics model has two important limitations. Firstly, no size distribution was considered, meaning that only the volume-averaged apparent crystallite size is determined. Secondly, as reported by Langford *et al.* (2000) and Popa & Balzar (2002) by analysis of ceria samples containing a size distribution of spherical crystallites, the Lorentzian is in general an unsatisfactory approximation for the size-broadened peak profile. Consequently, the model must be improved by using a better approximation for the size-broadened peak profile and allowing the determination of

both volume- and area-averaged apparent crystallites. This improvement is presented in the next section. In §3 the improved spherical harmonic model is used to fit a difficult X-ray diffraction pattern measured on a sample of zinc oxide. Finally, in §4, we show how the apparent crystallites determined by the whole powder pattern fitting (WPPF) using spherical harmonics can be interpreted in terms of some physical models by using ellipsoidal and cylindrical crystallites with lognormal size distributions.

2. Improving the model of spherical harmonics

The improved spherical harmonics model is achieved by including anisotropy in the model of spherical crystallites with lognormal size distribution.

In the past decade the model of spherical crystallites with lognormal size distribution has been the object of a number of publications. Krill & Birringer (1998) proposed to calculate the parameters of distribution, the mean radius $\bar{R}$ and the dispersion σ^2, by using the volume- and area-averaged column lengths determined from the Fourier coefficients of the diffraction peak obtained after Stokes deconvolution and separation of the strain contribution by the Warren–Averbach (Warren & Averbach, 1952) method. Ungár et al. (2001) also used the Fourier-space approach via the least-squares fitting of the analytical expressions containing both strain and size distribution parameters. Fourier analysis, in general, requires no peak overlap, a condition that is normally not fulfilled in diffraction patterns of nanocrystallite samples. In this case, a much more appropriate method to determine the size distribution parameters is whole powder pattern fitting (including Rietveld refinement). This method was first applied by Langford et al. (2000) to the X-ray diffraction pattern of a cerium oxide sample, assuming normal and lognormal size distributions. For both distributions the peak profile cannot be expressed by elementary functions; therefore, the authors calculated the profile by a numerical quadrature, which is a time-consuming process and thus not preferred for implementation in existing Rietveld codes. The authors observed that not only the peak breadth but also the peak shape depends on the distribution dispersion. As a quantitative measure, they defined the peak shape parameter φ by the ratio between the full width at half-maximum and the integral breadth. From the dependence of φ on the ratio $\sigma/\bar{R}$ the authors concluded that 'for a narrow distribution of size, the line-profile shape is intermediate between Lorentzian and Gaussian, and that it tends to become more Lorentzian in character as $\sigma/\bar{R}$ increases' (see Fig. 2 of their paper). Concerning the super-Lorentzian line profiles sometimes reported, it is considered that such an effect can arise when there is a bimodal distribution of size (Young & Sakthivel, 1988). Popa & Balzar (2002) also adopted whole pattern fitting to determine the parameters of the size distributions of spherical crystallites. Two distributions were considered, lognormal and gamma. To parametrize the distributions, the mean radius $\bar{R}$ and, in place of the dispersion σ^2, the relative dispersion $c = \sigma^2/\bar{R}^2$ were used. In this way, the size-

broadened peak shape depends only on c, and not on both σ^2 and $\bar{R}$. The peak shape can be calculated only by numerical quadrature; this method requires a large number of nodes,[1] which makes it prohibitive for implementation in Rietveld codes because of time considerations. Fortunately, the dependence of the size-broadened peak shape on only one parameter makes finding an analytical approximation possible. For the gamma distribution, c is physically limited to the range (0, 1) and the peak shape is very well approximated by a pseudo-Voigt function. For the lognormal distribution, c is in principle unlimited, but the authors searched for an approximation in the range (0, 6), which covers most of the situations found in practice; by comparison, Langford et al. (2000) considered only the range (0, 0.25). In this extended range the size-broadened peak shape was approximated by a sum of two or three Gauss and/or Lorentz functions (see Appendix A). This approximation makes the implementation in existing Rietveld codes simple. Indeed, the strain-broadened and instrumental peak profiles for most diffractometers can be described by Gauss, Lorentz, pseudo-Voigt, Voigt or linear combinations of these functions. Consequently, the convolution of all broadening effects can be performed analytically, resulting in a sum of Voigt[2] functions. The authors used this approach to fit the patterns of two cerium oxide samples, one of them exhibiting super-Lorentzian peak profiles. The authors also calculated the peak shape parameters φ as a function of c for both distributions. These are given in Fig. 2 of Popa & Balzar (2002). For the lognormal distribution the curve $\varphi(c)$ crosses the Lorentzian limit $\varphi = 0.6466$ at $c \simeq 0.5$, decreasing to $\varphi = 0.2856$ when $c = 6$. Therefore, for spherical crystallites with lognormal size distribution and $c > 0.5$, the peak shape is super-Lorentzian, and this character increases with increasing c. On the other hand, in the range $c \in (0, 0.4)$ the shape is well approximated by a pseudo-Voigt function (see Appendix A). For $c = 0$ the weight of the Gaussian component is equal to 0.75, but it is only 0.12 for $c = 0.4$. It can be concluded that the model of spherical crystallites with lognormal size distribution exhibits a wide variety of peak profiles, from near Gaussian profiles at small values of c, passing through near Lorentzian profiles, up to super-Lorentzian profiles with very sharp peak maxima and very long tails for large c.

This flexibility in the size-broadened line profile makes the model of spherical crystallites with lognormal size distribution a very convenient model to extend to the general anisotropic case. The distribution parameters $\bar{R}$ and c are replaced by functions dependent on direction, $\bar{R}_\mathbf{h}$ and $c_\mathbf{h}$, and then the size-broadened peak profile and the volume- and area-averaged column lengths [equations (15a), (12) and (13) of Popa & Balzar (2002)] become[3]

---

[1] The interference function is 'difficult' to integrate because the higher-order derivatives have a strongly oscillatory behavior. Consequently, to reach a given accuracy in a Gauss quadrature, a large number of nodes are necessary.
[2] Usually, to speed up the calculations in the Rietveld codes, the Voigt function is replaced by a pseudo-Voigt one (Thompson et al., 1987).
[3] The replacement is also performed in the Fourier transform of the peak profile [equation (14) of Popa & Balzar (2002)], but we do not give the expression for $\tilde{\psi}(\mathbf{r}, \mathbf{h})$ because it is not used in this paper.

$$\bar{P}(s, \mathbf{h}) = (3\bar{R}_{\mathbf{h}}/2)(1 + c_{\mathbf{h}})^3\, \bar{\Phi}(2\pi s\bar{R}_{\mathbf{h}}; c_{\mathbf{h}}), \quad s = 2\sin\theta/\lambda - 1/d, \tag{1}$$

$$D_{\mathrm{V}}(\mathbf{h}) = \bar{P}(0, \mathbf{h}) = (3\bar{R}_{\mathbf{h}}/2)(1 + c_{\mathbf{h}})^3, \tag{2}$$

$$D_{\mathrm{A}}(\mathbf{h}) = -1/\bar{\psi}'(0, \mathbf{h}) = (4\bar{R}_{\mathbf{h}}/3)(1 + c_{\mathbf{h}})^2. \tag{3}$$

The exact expression and the analytical approximation of the function $\bar{\Phi}(x; c)$ from equation (1) are reproduced in Appendix A. Concerning $\bar{R}_{\mathbf{h}}$ and $c_{\mathbf{h}}$, the unique necessary condition for these functions is to be invariant to the Laue group operations. Consequently, they can be expanded in series of symmetrized spherical harmonics:

$$\bar{R}_{\mathbf{h}} = \sum_{l=0}^{\infty} \sum_{m\in[0,\,l]} R_l^m K_l^m(\Phi, \beta), \tag{4}$$

$$c_{\mathbf{h}} = \sum_{l=0}^{\infty} \sum_{m\in[0,\,l]} c_l^m K_l^m(\Phi, \beta). \tag{5}$$

In these equations, R_l^m and c_l^m are refinable parameters in the whole pattern fitting and $K_l^m(\Phi, \beta)$ are the symmetrized spherical harmonics, Φ and β being the polar and azimuthal angles of $\mathbf{h}$ in a crystal orthogonal coordinate system. The symmetrized spherical harmonics for any Laue group are given by Popa (1992).

If the 'source' model of spherical crystallites with lognormal size distribution is a physical one, the previously described extension to anisotropy is purely phenomenological. This does not mean that the size distribution along $\mathbf{h}$ is lognormal with parameters $\bar{R}_{\mathbf{h}}$ and $c_{\mathbf{h}}$, but that the peak profile in this direction as well as its Fourier transform are close to those produced by spherical crystallites with such a distribution. Although the new model of spherical harmonics is, like the old model, a phenomenological one, it has by comparison three major advantages: (i) it describes the dependence on $\mathbf{h}$ not only of the peak breadth but also of the peak shape; (ii) it allows the determination of both volume- and area-averaged apparent crystallites; (iii) it can fit patterns exhibiting super-Lorentzian peak shapes.

The implementation of the improved model of spherical harmonics in the whole pattern fitting codes is identical to those of its source model, except for the number of refinable size parameters, unknown beforehand for the former. This number is determined by successive refinements, starting from the isotropic state and adding terms one by one to the series [equations (4) and (5)] until the reliability factors show no further significant improvement. Care must be taken concerning the series truncation because introduction of additional unneeded terms may produce ripples in the apparent crystallites determined from the fit.

In the next section we use the improved spherical harmonic model to fit, using the Pawley (1981) method, an X-ray diffraction pattern measured on a sample of zinc oxide. It is a difficult pattern, exhibiting a strong anisotropic size-broadening effect and strongly overlapped peaks of super-Lorentzian shapes. Moreover, a small but also anisotropic strain-broadening effect is detected.

3. Application of the improved model to an X-ray pattern of zinc oxide

3.1. Sample preparation and diffraction data collection

The ZnO powder was obtained by the thermal decomposition (in vacuum at 553 K) of zinc hydroxide nitrate, $Zn_3(OH)_4(NO_3)_2$. To obtain minimal strain, small masses of the precursor were used (see Auffrédic & Louër, 1987). Powder data were collected with a D500 Siemens high-resolution powder diffractometer with a Bragg–Brentano geometry and monochromatic Cu $K\alpha_1$ radiation (see Louër & Langford, 1988). The ZnO powder was deposited on an oriented Si crystal plate with low background. The diffraction pattern was scanned over the range 20–150° in 2θ, with a step of 0.02° and a counting time of 80 s per step. The NIST standard reference material SRM 660a LaB$_6$ was used to characterize the instrumental function. In the range 20–150° in 2θ, diffraction data for LaB$_6$ were collected only in 18 short segments around each peak. Depending on the peak breadth and peak intensity, these segments were scanned with a step length of between 0.006 and 0.02° ($\sim$FWHM/10), and the scan ranges (20–30 × FWHM) were roughly constant on a d^{-1} scale. The counting time per step was between 40 and 180 s. All ranges can be put in a single pattern by normalizing to unit time both the intensities and the standard uncertainties.

3.2. Fitting LaB$_6$ data

To find the analytical representation of the instrumental profiles from LaB$_6$ data, three types of fits were necessary. A preliminary data analysis including the peak asymmetry showed that the asymmetry parameter is significant only for the first peak, (100) at $2\theta \simeq 21.36°$, whereas the rest, beginning with (110) at $2\theta \simeq 30.38°$, are perfectly symmetrical. Fortunately, the first peak in the ZnO pattern is at $2\theta \simeq 31.77°$, which allowed us to exclude the (100) peak of LaB$_6$ from the subsequent analysis. For the other peaks, the measured data in each range were fitted by a Voigt function plus a linear background. There are six fitting parameters for a range: two parameters for background, the peak area $s_{\mathbf{H}}$, the peak position $2\theta_m$, and the integral breadths of the Gaussian and Lorentzian components of the Voigt function, β_{IG} and β_{IL}, respectively. The index I here denotes an instrumental profile. In the second step the values of the peak positions and of the integral breadths determined from the single peak fits were used in a least-squares fitting program to find their analytical dependence on the Bragg angle, $\theta_{\mathbf{H}} = \arcsin(\lambda/2d_{\mathbf{H}})$. For the peak position we have found the following expression:

$$2\theta_m(\theta_{\mathbf{H}}) = (180/\pi)\,2\theta_{\mathbf{H}} + \delta_0 + \delta_1 \cot\theta_{\mathbf{H}} + \delta_2 \sin 2\theta_{\mathbf{H}}. \tag{6}$$

Here the last three terms represent the diffractometer zero, flat specimen and sample transparency peak shifts. For the integral breadths of the Voigt function components the best fits were obtained with the following polynomials in $\tan\theta_{\mathbf{H}}$:

$$\beta_{\mathrm{IG}}(\theta_{\mathbf{H}}) = \beta_{g0} + \beta_{g1}\tan\theta_{\mathbf{H}} + \beta_{g2}\tan^2\theta_{\mathbf{H}} + \beta_{g3}\tan^3\theta_{\mathbf{H}}, \tag{7}$$

Table 1
The instrumental breadth parameters in equations (7) and (8) refined by the Pawley fit of the LaB_6 diffraction pattern; the reliability factors are included.

i	$10^2 \beta_{gi}$	$10^2 \beta_{li}$
0	5.94 (3)	–
1	0.88 (12)	1.05 (8)
2	0.48 (13)	3.12 (19)
3	−0.20 (3)	−0.68 (11)
4	–	0.06 (2)
	$R_p = 3.86\%$	$R_{wp} = 5.30\%$

$$\beta_{IL}(\theta_{\mathbf{H}}) = \beta_{l1} \tan \theta_{\mathbf{H}} + \beta_{l2} \tan^2 \theta_{\mathbf{H}} + \beta_{l3} \tan^3 \theta_{\mathbf{H}} + \beta_{l4} \tan^4 \theta_{\mathbf{H}}. \tag{8}$$

In the third step a Pawley-type whole powder pattern fitting was performed with the following calculated intensity:

$$I(2\theta) = B(2\theta) + \sum_{\mathbf{H}} s_{\mathbf{H}} V(2\theta - 2\theta_m; \beta_{IG}, \beta_{IL}). \tag{9}$$

Here V is the Voigt function (normalized to unit area) and $B(2\theta)$ is the background, for which we used a five-degree polynomial in 2θ. There are 35 refined parameters, but only β_{gi} ($i = 0, 1, 2, 3$) and β_{li} ($i = 1, 2, 3, 4$) from equations (7) and (8) are important for the next section. These are given in Table 1, together with the reliability factors of the fit. The integral breadths β_{IG} and β_{IL} calculated with these parameters are shown in Fig. 1, together with the Voigt integral breadth $\beta_I = \beta_{IG}^{-1} \exp(r^2) \operatorname{erfc}(r)$, where $r = \beta_{IL}/\beta_{IG}\pi^{1/2}$. This variation of Voigt integral breadths with $\tan\theta$ is comparable to that reported for the BaF_2 standard material with the same instrument (Fig. 7 in Louër & Langford, 1988). Finally, zooms on three peaks from the LaB_6 diffraction pattern fitted by equation (9) are shown in Fig. 2.

3.3. The Pawley fit of the zinc oxide pattern

For the angular dispersive diffraction method we must set $s = (\cos \theta_{\mathbf{H}}/\lambda)\Delta 2\theta$ in equation (1). Considering for $\bar{\Phi}$ the analytical approximation (30), the peak profile $\bar{P}_{\mathbf{H}}(\Delta 2\theta) =$

$\bar{P}(s, \mathbf{h})| \, \mathrm{d}s/\mathrm{d}(\Delta 2\theta)|$ will be a sum of two or three Gauss and/or Lorentz functions with the following integral breadths:

$$\beta_{Sj}(\theta_{\mathbf{H}}) = (180/\pi) \lambda/[4\bar{R}_{\mathbf{h}} \cos \theta_{\mathbf{H}} \alpha_j(c_{\mathbf{h}})] \quad (j = 1, 3). \tag{10}$$

In this equation the index S denotes a size quantity and the functions $\alpha_j(c_{\mathbf{h}})$ are given in Appendix A. Concerning the strain effect, according to Popa (1998), the contribution to the integral breadth of the peak profile is

(a)

(b)

(c)
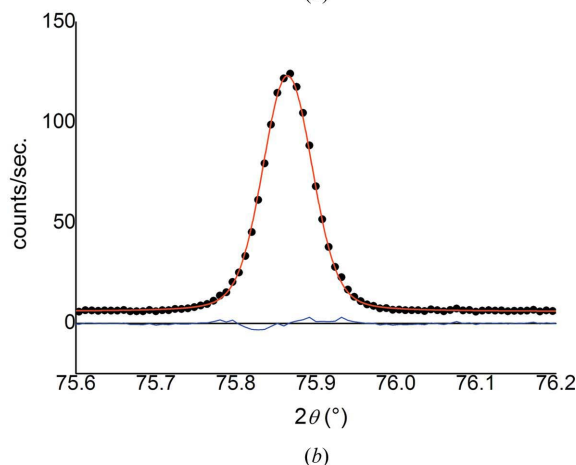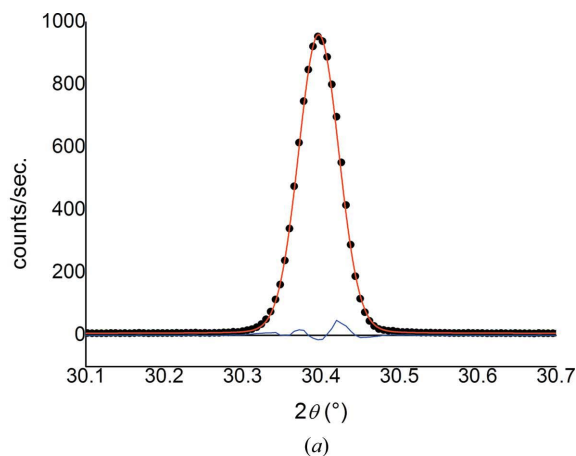
Figure 2
Pawley fits with Voigt profiles of the LaB_6 diffraction pattern: zooms in an angular range of 0.6° on three peaks, at small (a), medium (b) and high (c) scattering angles.
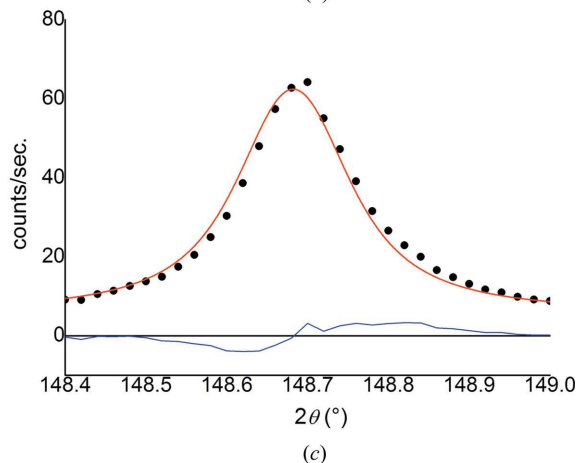

Figure 1
Instrumental integral breadths β_{IG}, β_{IL} and β_I versus $\tan \theta_{\mathbf{H}}$ obtained from the Pawley fit with equation (9) of an LaB_6 diffraction pattern in the range $30 \leq 2\theta_{\mathbf{H}} \leq 150°$.

Table 2
The size parameters R_l^m and c_l^m and the strain parameters E_i refined by the Pawley fit of the zinc oxide diffraction pattern; the reliability factors are included.

R_l^m	c_l^m	$E_i,\ R_p,\ R_{wp}$
$R_0^0 = 23.53\,(13)$	$c_0^0 = 1.826\,(11)$	$E_1 = 0.0208\,(2)$
$R_2^0 = -11.56\,(11)$	$c_2^0 = 0.917\,(15)$	$E_2 = 0.0058\,(7)$
$R_4^0 = 3.52\,(3)$	$c_4^0 = 0.162\,(5)$	$E_3 = 0$
$R_6^0 = 0$	$c_6^0 = 0$	$R_p = 4.77\%$
$R_6^6 = -7.70\,(15)$	$c_6^6 = 0.121\,(4)$	$R_{wp} = 6.46\%$

$$\beta_E(\theta_{\mathbf{H}}) = (180/\pi)\,2\tan\theta_{\mathbf{H}}\,(2\pi\langle\varepsilon_{\mathbf{h}}^2\rangle)^{1/2}. \tag{11}$$

Here $\langle\varepsilon_{\mathbf{h}}^2\rangle$ is the dispersion of the strain distribution, considered to be Gaussian. As the instrumental profile is a Voigt function, the calculated intensity used in the Pawley fitting of the zinc oxide pattern is the following:

$$I(2\theta) = B(2\theta) + \sum_{\mathbf{H}} s_{\mathbf{H}} \sum_{j=1}^{3} \eta_j(c_{\mathbf{h}}) V(2\theta - 2\theta_m; \beta_{Gj}, \beta_{Lj}). \tag{12}$$

For background we used a six-degree polynomial in 2θ, the functions $\eta_j(c_{\mathbf{h}})$ can be found in Appendix A, $2\theta_m$ is given by
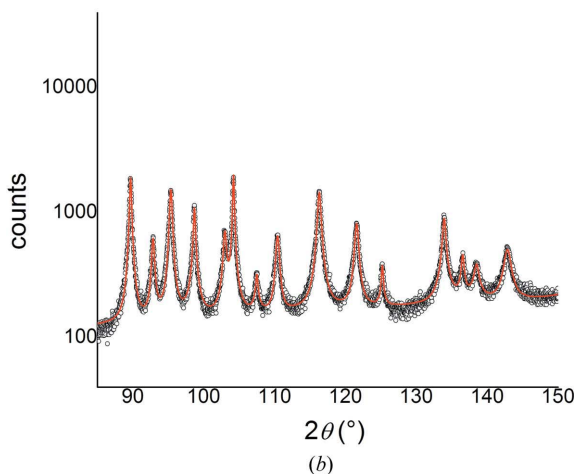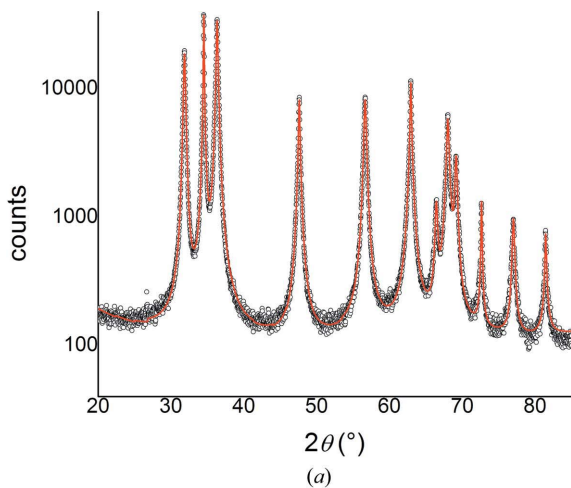

(a)

(b)

Figure 3
Pawley fits of the ZnO diffraction pattern: (a) the range $(20°, 85°)$, (b) the range $(85°, 150°)$.

equation (6), and β_{Gj} and β_{Lj} are calculated from equations (7), (8), (10) and (11) as follows:

$$\beta_{Gj}(\theta_{\mathbf{H}}) = \left(\beta_{IG}^2 + \beta_E^2\right)^{1/2} \quad (j = 1, 2),$$

$$\beta_{Lj}(\theta_{\mathbf{H}}) = \beta_{IL} + \beta_{Sj} \quad (j = 1, 2),$$

$$\beta_{G3}(\theta_{\mathbf{H}}) = \begin{cases} (\beta_{IG}^2 + \beta_E^2 + \beta_{S3}^2)^{1/2} & \text{if } 0 \le c_{\mathbf{h}} \le 1 \\ (\beta_{IG}^2 + \beta_E^2)^{1/2} & \text{if } 1 \le c_{\mathbf{h}}, \end{cases}$$

$$\beta_{L3}(\theta_{\mathbf{H}}) = \begin{cases} \beta_{IL} & \text{if } 0 \le c_{\mathbf{h}} \le 1 \\ \beta_{IL} + \beta_{S3} & \text{if } 1 \le c_{\mathbf{h}}. \end{cases}$$

The Laue group of zinc oxide is $6/mmm$; then, according to Popa (1998), equations (4) and (5) become

$$\bar{R}_{\mathbf{h}} = R_0^0 P_0^0(\Phi) + R_2^0 P_2^0(\Phi) + R_4^0 P_4^0(\Phi) + R_6^0 P_6^0(\Phi) + R_6^6 P_6^6(\Phi)\cos 6\beta + \cdots, \tag{13}$$

$$c_{\mathbf{h}} = c_0^0 P_0^0(\Phi) + c_2^0 P_2^0(\Phi) + c_4^0 P_4^0(\Phi) + c_6^0 P_6^0(\Phi) + c_6^6 P_6^6(\Phi)\cos 6\beta + \cdots. \tag{14}$$

In these equations $P_l^m(\Phi)$ are normalized Legendre functions. According to the same paper the strain dispersion $\langle\varepsilon_{\mathbf{h}}^2\rangle$ can be written by using quartic forms in h, k, l, invariant to the Laue group operations. Alternatively, we can use linear combinations of symmetrized homogenous polynomials of the fourth degree in a_1, a_2, a_3, the direction cosines of $\mathbf{h}$ in the crystal orthogonal coordinate system.[4] For the Laue group $6/mmm$ we have

$$\langle\varepsilon_{\mathbf{h}}^2\rangle = E_1(a_1^2 + a_2^2)^2 + E_2 a_3^4 + 2E_3(a_1^2 + a_2^2)a_3^2. \tag{15}$$

The direction cosines a_1, a_2, a_3 as well as the polar and azimuthal angles Φ and β of $\mathbf{h}$ can be calculated from the Miller indices and the lattice constants. The crystal orthogonal coordinate system is defined by $\mathbf{x}_3 = \mathbf{c}/c$, $\mathbf{x}_1 = \mathbf{a}/a$, $\mathbf{x}_2 = \mathbf{x}_3 \times \mathbf{x}_1$, and then we have

$$a_1 = \sin\Phi\cos\beta = h\,d_{\mathbf{H}}/a,$$

$$a_2 = \sin\Phi\sin\beta = (h + 2k)\,d_{\mathbf{H}}/(3^{1/2}a),$$

$$a_3 = \cos\Phi = l\,d_{\mathbf{H}}/c.$$

The size–strain broadening parameters R_l^m, c_l^m and E_i in equations (13), (14) and (15) obtained by fitting equation (12) with the measured pattern of zinc oxide are given in Table 2, together with the reliability factors of the fit. The fitted pattern is shown in Fig. 3. The logarithmic scale for intensity in this figure emphasizes how strongly the peaks are overlapped. Zooms on four peaks in identical angular intervals are given in Fig. 4. Large differences in breadths are evident. The parameters of the 'equivalent' lognormal distributions of spherical crystallites $\bar{R}_{\mathbf{h}}$ and $c_{\mathbf{h}}$, the volume- and area-averaged column lengths $D_V(\mathbf{h})$ and $D_A(\mathbf{h})$, and the strain $\langle\varepsilon_{\mathbf{h}}^2\rangle^{1/2}$ calculated with equations (13), (14), (2), (3) and (15) from the refined size–

---

[4] The complete sets of homogenous polynomials of two, four and six degrees in a_1, a_2, a_3, symmetrized for all Laue groups, are given by Popa & Balzar (2001).

research papers

strain parameters are given in Table 3 as a function of *hkl*. Three things follow from this table: (i) the values of $c_{\mathbf{h}}$ are always greater than 0.5, which means that all peaks are super-Lorentzian; (ii) the averaged column lengths are strongly anisotropic, the ratio between the maximum and minimum values being 3.45 for D_V and 1.94 for D_A; (iii) the strain is small ($\langle\varepsilon^2\rangle_{max}^{1/2} = 5.02 \times 10^{-4}$) and anisotropic. Finally, in Figs. 5(*a*) and 5(*b*) are given the cross sections of the volume- and area-averaged apparent crystallites within the **ab** and **ac** planes, respectively. The peculiarities of these cross sections will be discussed later in §4.4.

4. Interpretation of the apparent crystallites in terms of 'physical' models

Most users of the Rietveld programs are interested in structure refinement and for these users phenomenological models for microstructure that achieve a good pattern fit are sufficient. However, if one wants to know more detailed micro-structural information besides features of the apparent crystallites, the shape (morphology), orientation and size distributions of the real crystallites need to be determined. It

Table 3
The volume- and area-averaged column lengths (Å) and the micro-strain as a function of (*hkl*) (higher orders excluded).

The parameters of the 'equivalent' lognormal distributions of spherical crystallites are given in columns 3 and 4.

|	*hkl*	$\bar{R}_{\mathbf{h}}$	$c_{\mathbf{h}}$	$D_V(\mathbf{h})$	$D_A(\mathbf{h})$	$10^4\langle\varepsilon_{\mathbf{h}}^2\rangle^{1/2}$
1	100	37.90	0.5489	211 (6)	121 (3)	5.02 (3)
2	002	5.82	3.0862	596 (24)	130 (5)	2.66 (16)
3	101	22.04	0.9043	228 (4)	107 (1)	3.93 (2)
4	102	9.11	1.5949	239 (4)	82 (1)	2.72 (5)
5	110	19.25	0.8424	181 (5)	87 (2)	5.02 (3)
6	103	5.76	2.1236	264 (8)	75 (2)	2.37 (9)
8	112	12.13	1.1164	173 (3)	72 (1)	3.69 (2)
9	201	32.50	0.6439	217 (5)	117 (2)	4.68 (2)
12	104	5.14	2.4453	315 (11)	81 (2)	2.36 (12)
13	203	13.78	1.2508	236 (4)	93 (1)	3.21 (2)
14	210	24.69	0.7569	201 (5)	102 (2)	5.02 (3)
15	211	22.97	0.7876	197 (5)	98 (2)	4.82 (2)
16	114	6.38	1.8016	210 (5)	67 (1)	2.54 (6)
17	212	18.87	0.8913	192 (3)	90 (1)	4.32 (2)
18	105	5.12	2.6384	370 (14)	90 (3)	2.41 (13)
21	213	14.38	1.0727	192 (3)	82 (1)	3.72 (2)
22	302	29.10	0.7153	220 (5)	114 (2)	4.45 (2)
24	205	6.82	1.8891	247 (6)	76 (2)	2.47 (7)
25	106	5.21	2.7590	415 (16)	98 (4)	2.47 (14)
26	214	10.78	1.3041	198 (3)	76 (1)	3.19 (3)
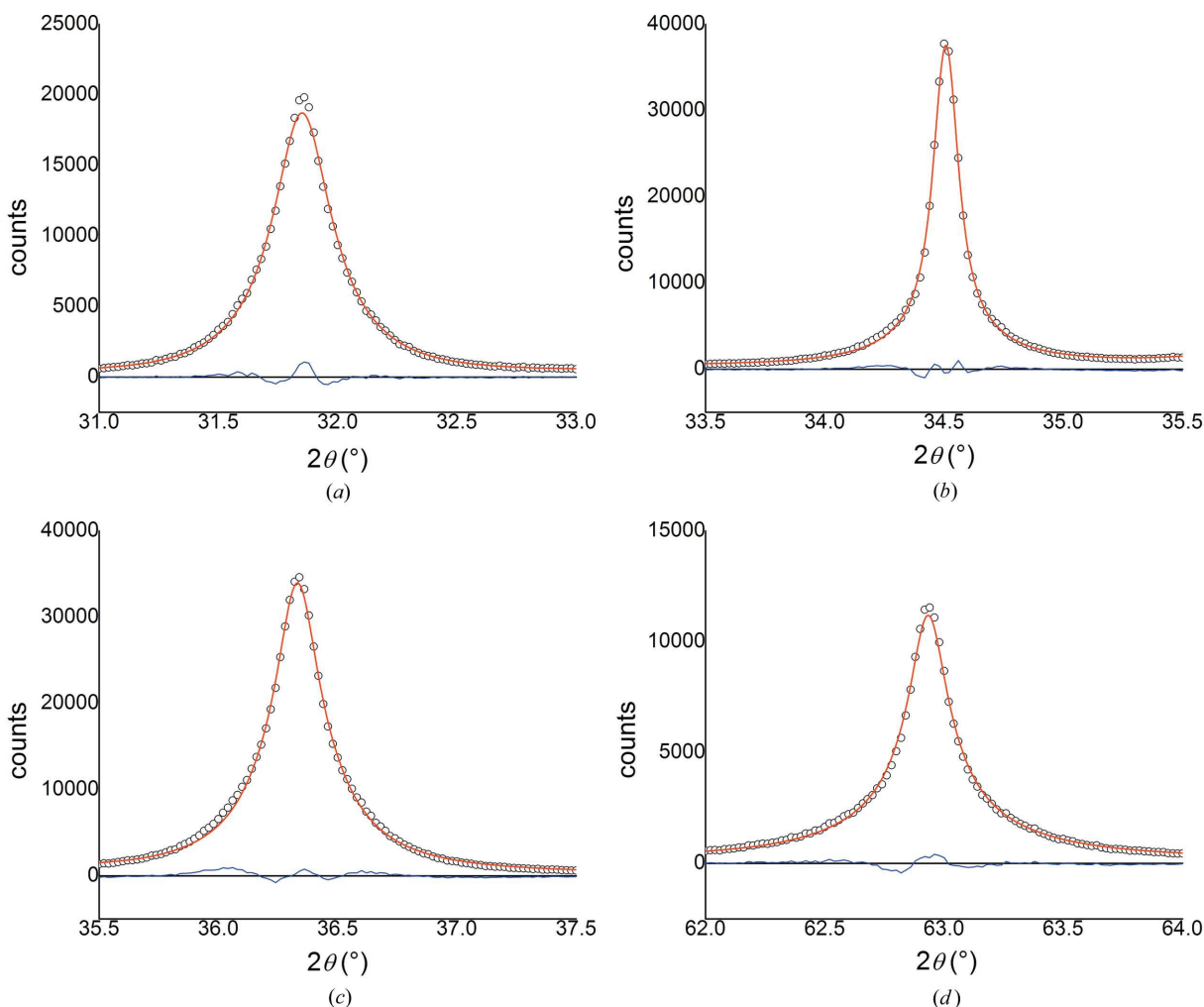
Figure 4
Zooms in an angular interval of 2° of four peaks from the fitted ZnO pattern: (*a*) (100), (*b*) (002), (*c*) (101) and (*d*) (103).
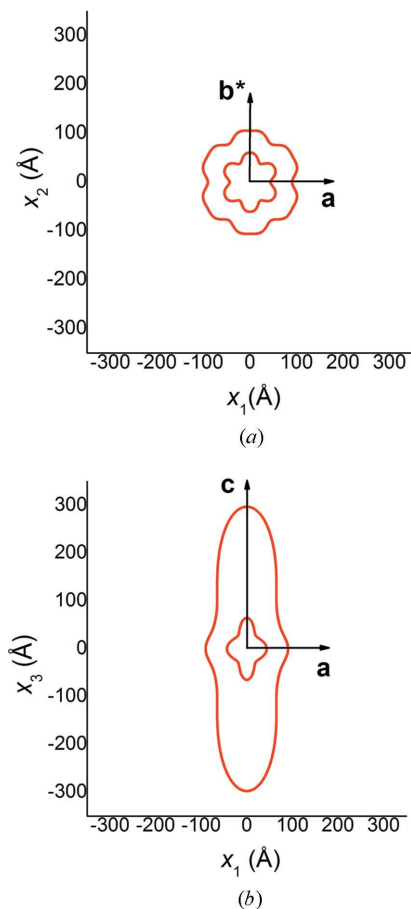
Figure 5
Two cross sections of the apparent crystallites: (*a*) in the *ab* plane (equatorial) and (*b*) in the *ac* plane (vertical). Outer contour: volume-averaged apparent crystallite; inner contour: area-averaged apparent crystallite.

should be outlined that, in principle, the diffraction pattern does not contain enough information to determine these microstructure details unequivocally. Diffraction line-broadening analysis yields only the parameters of an *a priori* physically based crystallite size model. This seems to be a simple task at first sight. Starting from a given model for crystallite shape, orientation and size distributions, one calculates the peak profiles for the apparent crystallites. Then the model parameters are found by fitting the calculated pattern to the measured one or by fitting the calculated apparent crystallites with those derived from the measured data (see details in the next section). Both the peak profiles and the apparent crystallites are integral quantities resulting from a number of averages, which means that finding the model parameters involves an inverse problem. If these problems are ill-posed to a certain degree, then a solution may not be unique. An example confirming this statement was reported by Popa & Balzar (2002): two different size distributions of spherical crystallites, lognormal and gamma, with significantly different mean radii and relative dispersions produced equally good fits of a cerium oxide pattern and very similar apparent crystallites. For nonspherical crystallites the

number of model parameters is greater than two, and multiple solutions may occur not only among different models but also within a given model. To minimize this occurrence, simple models are preferable, although they might describe real crystallites only approximately. It is also very important to use some *a priori* information that allows the fixing or constraint of a number of parameters. Even with these precautions, additional information obtained by other experimental techniques (such as transmission electron microscopy, TEM) is necessary to be fully confident in a solution. The diffraction alone is probably limited to reliably providing only the shapes and sizes of the apparent crystallites.

It should be mentioned here that there are a few less biased approaches for line-broadening analysis, such as Fourier deconvolution followed by the Warren–Averbach (Warren & Averbach, 1952) method, that yield $D_V(\mathbf{h})$ and $D_A(\mathbf{h})$, as well as both the column length and crystallite size distribution, without *a priori* assuming a model for the crystallite size distribution. Moreover, Leoni & Scardi (2004) demonstrated the whole powder pattern modeling (WPPM) approach without assuming an *a priori* model for the crystallite size distribution. However, if the parameters of the physical crystallite size distribution are to be determined, these approaches are difficult to implement, especially for patterns with significant peak overlap, and give uncertain results owing to significant error propagation. Krill & Birringer (1998) and later Langford *et al.* (2000) followed a different approach by assuming an *a priori* lognormal crystallite size distribution. For spherical crystallites, the size-broadened profile is then defined by only two parameters of the lognormal crystallite size distribution: mean radius $\bar{R}$ and the distribution dispersion σ^2 (instead, we use the relative dispersion $c = \sigma^2/\bar{R}^2$). Krill & Birringer (1998) showed that instead of using $\bar{R}$ and c, D_V and D_A give an equivalent representation of both the size-broadened profile and the crystallite size distribution. Therefore, $\bar{R}$ and c uniquely correspond to D_V and D_A, which also uniquely define the whole size-broadened profile. Therefore, under the same *a priori* assumption (for instance, a given crystallite size distribution) and comparable goodness of fit, both the WPPF and the WPPM approaches should yield identical results within a single standard uncertainty, as not only D_V and D_A but also the peak profile itself are uniquely defined by the size-distribution parameters. Moreover, as finding the model parameters involves an inverse problem and these problems are sometimes ill-posed, a solution may not be unique in either approach.

Making an assumption on the actual size distribution is obviously critical. Complementary information obtained by transmission or scanning electron microscopy or by similar techniques is always helpful but also can give ambiguous results, in particular for narrow and symmetric size distributions. Another size distribution that was considered by several authors is the gamma distribution. Popa & Balzar (2002) studied both distributions and concluded that only the lognormal distribution is able to fit the super-Lorentzian line profiles that are present in the diffraction patterns discussed here.

4.1. Fitting averaged column lengths *versus* whole powder pattern fitting

There are three possible ways to find the shape, orientation and size distributions of crystallites, two of them involving whole powder pattern fitting. Scardi & Leoni (2002, 2006) recommend the WPPM approach, meaning that the pattern fitting the diffraction data is calculated exactly starting from parametrized physical models for all components of the peak profile. In general, a Rietveld code using this method is time consuming and not attractive for either the code providers or most users. In particular, the nonspherical crystallites are characterized by $n > 1$ independent parameters with a distribution for each one. The size peak profile results after n averages over distributions, most of them calculated by numerical integration, plus one average over the equivalents of **h**, which significantly slows down the refinement. The execution time can be significantly reduced if a hybrid method is used in place of the whole pattern modeling. This is a whole pattern fitting with a predetermined profile but with profile parameters calculated from a physical model. Explicitly, we can use equation (1) for the size profile,[5] but in place of $\bar{R}_\mathbf{h}$ and $c_\mathbf{h}$ we use their expressions derived from equations (2) and (3) with the column lengths $D_V(\mathbf{h})$ and $D_A(\mathbf{h})$ derived from physical anisotropic size models. In this way the $n+1$ averages discussed previously are transferred from the peak profile to the profile parameters, thus making the fit significantly faster. Nevertheless this fit is slower than those using spherical harmonics, which require no averaging. Moreover, one expects any type of whole pattern fitting using models for crystallite shape to be less successful than those using spherical harmonics, because these models have an idealized character. A worse fit means less confidence in other refined parameters. Therefore, in our opinion, it is preferable to determine the parameters of a physical anisotropic size model outside of a whole pattern fitting program, by minimizing the following function:[6]

$$\chi^2 = \sum_{V,A,\mathbf{h}} w \left[D_{V,A}^{sph}(\mathbf{h}) - D_{V,A}^{cal}(\mathbf{h}) \right]^2. \quad (16)$$

Here $D_{V,A}^{sph}(\mathbf{h})$ are the volume- and area-averaged column lengths obtained from the whole pattern fitting using the model of spherical harmonics and $D_{V,A}^{cal}(\mathbf{h})$ are the column lengths calculated from physical models. We adopt this approach in the present paper.

4.2. Calculation of the averaged column lengths: the general algorithm

Two out of the three approaches to find the shape, orientation and size distributions of crystallites described in the previous section require the calculation of the averaged column lengths $D_V(\mathbf{h})$ and $D_A(\mathbf{h})$. Let us denote by **S** the

vector of $n > 1$ independent parameters describing non-spherical crystallites with a given shape. These parameters are some specific lengths and some angles giving the crystallite orientation with respect to the crystal orthogonal system $(\mathbf{x}_1, \mathbf{x}_2, \mathbf{x}_3)$. In principle each parameter may have a distribution of values, and in general we must introduce an n-dimensional distribution function $f(\mathbf{S})$. Any quantity depending on the crystallite shape, size and orientation is calculated by averaging over this distribution.

The calculation of the averaged column lengths is performed in three steps.

(i) Firstly, we calculate the Fourier transform of the size profile for a given vector **S**. For a powder sample it can be written as follows:

$$\psi(r, \mathbf{h}) = n_\mathbf{h}^{-1} \sum_{k=1}^{n_\mathbf{h}} \begin{cases} \psi_0(r, \mathbf{h}_k) & \text{if } 0 \leq r \leq R_{\mathbf{h}_k} + R_{-\mathbf{h}_k} \\ 0 & \text{if } r \geq R_{\mathbf{h}_k} + R_{-\mathbf{h}_k}. \end{cases} \quad (17)$$

In this equation $\mathbf{h}_k$ is the equivalent k of **h**, $n_\mathbf{h}$ is the total number of equivalents and $R_{\mathbf{h}_h}$ is the crystallite radius along $\mathbf{h}_k$. The function $\psi_0(r, \mathbf{h}_k)$ is the ratio between the volume common to the crystallite and its 'ghost' displaced at a distance r in the direction $\mathbf{h}_k$ and the crystallite volume V. The sum in equation (17) means the average over equivalents. In practice only half of the number of equivalents is considered because $\psi_0(r, -\mathbf{h}_k) = \psi_0(r, \mathbf{h}_k)$.

(ii) Secondly, we calculate the derivative of $\psi(r, \mathbf{h})$ at $r = 0$ and the height (maximum) of its Fourier transform $P(s, \mathbf{h})$:

$$\psi'(0, \mathbf{h}) = n_\mathbf{h}^{-1} \sum_{k=1}^{n_\mathbf{h}} \psi_0'(0, \mathbf{h}_k), \quad (18)$$

$$P(0, \mathbf{h}) = 2 \int_0^\infty \psi(r, \mathbf{h}) \, dr = 2n_\mathbf{h}^{-1} \sum_{k=1}^{n_\mathbf{h}} \int_0^{R_{\mathbf{h}_k} + R_{-\mathbf{h}_k}} \psi_0(r, \mathbf{h}_k) \, dr. \quad (19)$$

(iii) Finally, the averaged column lengths are calculated from equations (18) and (19) as follows:

$$D_A(\mathbf{h}) = -1/\bar{\psi}'(0, \mathbf{h}) = -\langle V \rangle / \langle V \psi'(0, \mathbf{h}) \rangle, \quad (20)$$

$$D_V(\mathbf{h}) = \bar{P}(0, \mathbf{h}) = \langle V P(0, \mathbf{h}) \rangle / \langle V \rangle. \quad (21)$$

The brackets in these equations denote the following average: $\langle F \rangle = \int F(\mathbf{S}) f(\mathbf{S}) \, d\mathbf{S}$.

4.3. Ellipsoids and elliptical cylinders with multimodal lognormal distributions and identical shape and orientation per mode

Both the ellipsoid and the elliptical cylinder are described by six independent parameters, the principal radii R_1, R_2 and R_3 (the cylinder height is $2R_3$), and the Euler angles ω, χ and φ giving the orientations of the principal axes $\mathbf{p}_1$, $\mathbf{p}_2$ and $\mathbf{p}_3$ with respect to the crystal orthogonal system: $\mathbf{p}_i = \sum_{j=1}^3 E_{ij}(\omega, \chi, \varphi) \mathbf{x}_j$. Here **E** is the Euler matrix. In principle, an independent distribution can be assigned to each parameter, but it is advisable to introduce some constraints to obtain simpler models with a smaller number of fitting parameters. For the principal radii the distributions can be those commonly used for spherical crystallites, such as lognormal or

---

[5] The arguments for using equation (1) for size anisotropy were discussed in §2.
[6] Strictly, a function accounting for the correlations of $D_{V,A}^{sph}(\mathbf{h})$ should be used in place of equation (16), but, considering that the inaccuracy caused by the ideal character of the shape models is probably larger, we can avoid this complication.

gamma. However, there is no similar analogy that would help choose a particular function for the Euler angle distributions. We know only that these distributions cannot be uniform in the range of definition: $[0, 2\pi]$ for ω and φ and $[0, \pi]$ for χ; otherwise the size effect is isotropic even if the crystallites are not spherical. To have size anisotropy the crystallite shape orientation must be preferential. In this paper we adopt the simplest preferential orientation: δ functions for the Euler angle distributions. For the principal radii the lognormal and gamma distributions have been considered in numerous publications, and the lognormal was shown to be the most realistic for modeling the distribution of crystallite sizes (see, for instance, Langford *et al.*, 2000; Popa & Balzar, 2002). Popa & Balzar (2002) showed that the gamma distribution cannot model super-Lorentzian peak profiles. As all peaks in the pattern of the actual sample of zinc oxide are super-Lorentzian we should limit our choice to the lognormal distribution. To obtain a simpler model we constrain the principal radii to have constant ratios. With this choice and presuming the distribution to be multimodal,[7] the distribution $f(\mathbf{S})$ can be written as follows:

$$f(\mathbf{S}) = \sum_m \big[\xi_m \delta(\omega - \bar{\omega}_m)\delta(\chi - \bar{\chi}_m)\delta(\varphi - \bar{\varphi}_m)$$
$$\times \delta(R_1 - \bar{r}_{m1}R_3)\delta(R_2 - \bar{r}_{m2}R_3)f_{\mathrm{L}}(R_3; \bar{R}_{m3}, c_m)\big]. \quad (22)$$

The index m counts the modes, ξ_m are the weights of modes fulfilling the condition $\sum_m \xi_m = 1$ and f_{L} is the lognormal distribution:

$$f_{\mathrm{L}}(R; \bar{R}, c) = R^{-1}[2\pi \ln(1+c)]^{1/2} \exp\left\{\frac{-\ln^2[R\bar{R}^{-1}(1+c)^{1/2}]}{[2\ln(1+c)]}\right\}.$$

Expression (22) describes the simplest model using ellipsoids or elliptical cylinders and allowing for size distribution: crystallites of identical shape and orientation per mode, differing from one another only by size. The model fitting parameters are ξ_m, $\bar{\omega}_m$, $\bar{\chi}_m$, $\bar{\varphi}_m$, $\bar{r}_{m1}$, $\bar{r}_{m2}$, $\bar{R}_{m3}$ and c_m. Once the model is defined we can calculate $D_{\mathrm{A}}(\mathbf{h})$ and $D_{\mathrm{V}}(\mathbf{h})$.

4.3.1. Ellipsoids. An ellipsoid can be transformed into a sphere by a linear scaling of axes. Following this reasoning the function ψ_0 of a sphere (see *e.g.* Popa & Balzar, 2002) can be extended to an ellipsoid by replacing the sphere radius with the ellipsoid radius. Then we have

$$\psi_0(r, \mathbf{h}_k) = 1 - \frac{3}{2}\frac{r}{2R_{\mathbf{h}_k}} + \frac{1}{2}\left(\frac{r}{2R_{\mathbf{h}_k}}\right)^3, \quad 0 \le r \le 2R_{\mathbf{h}_k}, \quad (23)$$

$$R_{\mathbf{h}_k}^{-1} = \big[(\mathbf{h}_k\mathbf{p}_1)^2/R_1^2 + (\mathbf{h}_k\mathbf{p}_2)^2/R_2^2 + (\mathbf{h}_k\mathbf{p}_3)^2/R_3^2\big]^{1/2}.$$

Furthermore we use equations (18), (19), (20) and (21) with $f(\mathbf{S})$ given by equation (22). For this model the average over $\mathbf{S}$ can be performed analytically and one obtains

$$D_{\mathrm{A}}(\mathbf{h}) = \frac{4}{3}\frac{\sum_m \xi_m \bar{r}_{m1}\bar{r}_{m2}\bar{R}_{m3}^3(1+c_m)^3}{\sum_m \xi_m \bar{r}_{m1}\bar{r}_{m2}\bar{R}_{m3}^2(1+c_m)n_{\mathbf{h}}^{-1}\sum_k \rho_{km}^{-1}}, \quad (24)$$

$$D_{\mathrm{V}}(\mathbf{h}) = \frac{3}{2}\frac{\sum_m \xi_m \bar{r}_{m1}\bar{r}_{m2}\bar{R}_{m3}^4(1+c_m)^6 n_{\mathbf{h}}^{-1}\sum_k \rho_{km}}{\sum_m \xi_m \bar{r}_{m1}\bar{r}_{m2}\bar{R}_{m3}^3(1+c_m)^3}, \quad (25)$$

$$\rho_{km}^{-1} = \big(h_{km1}^2/\bar{r}_{m1}^2 + h_{km2}^2/\bar{r}_{m2}^2 + h_{km3}^2\big)^{1/2},$$

$$h_{kmi} = \mathbf{h}_k\mathbf{p}_{mi}, \quad \mathbf{p}_{mi} = \sum_{j=1}^3 E_{ij}(\bar{\omega}_m, \bar{\chi}_m, \bar{\varphi}_m)\mathbf{x}_j.$$

4.3.2. Elliptical cylinders. Like the ellipsoid, the ellipse can be transformed into a circle and then, in a similar manner, the function ψ_0 of the circular cylinder (see Langford & Louër, 1982) can be extended to the elliptical cylinder:

$$\psi_0(r, \mathbf{h}_k) = \left\{1 - \frac{2}{\pi}\arcsin\left(\frac{r}{2R_{\mathbf{h}_k}^{\mathrm{t}}}\right) - \frac{2}{\pi}\frac{r}{2R_{\mathbf{h}_k}^{\mathrm{t}}}\left[1 - \left(\frac{r}{2R_{\mathbf{h}_k}^{\mathrm{t}}}\right)^2\right]^{1/2}\right\}$$
$$\times \left[1 - \frac{r}{2R_{\mathbf{h}_k}^{\mathrm{l}}}\right], \quad 0 \le r \le 2R_{\mathbf{h}_k}, \quad (26)$$

$$R_{\mathbf{h}_k} = \min(R_{\mathbf{h}_k}^{\mathrm{t}}, R_{\mathbf{h}_k}^{\mathrm{l}}),$$

$$1/R_{\mathbf{h}_k}^{\mathrm{t}} = \big[(\mathbf{h}_k\mathbf{p}_1)^2/R_1^2 + (\mathbf{h}_k\mathbf{p}_2)^2/R_2^2\big]^{1/2}, \quad 1/R_{\mathbf{h}_k}^{\mathrm{l}} = |\mathbf{h}_k\mathbf{p}_3|/R_3.$$

Combining equations (18), (19), (20) and (21) one obtains the following expressions:

$$D_{\mathrm{A}}(\mathbf{h}) = \frac{2\sum_m \xi_m \bar{r}_{m1}\bar{r}_{m2}\bar{R}_{m3}^3(1+c_m)^3}{\sum_m \xi_m \bar{r}_{m1}\bar{r}_{m2}\bar{R}_{m3}^2(1+c_m)n_{\mathbf{h}}^{-1}\sum_k \big[|h_{km3}| + (4/\pi)\sigma_{km}^{-1}\big]}, \quad (27)$$

$$D_{\mathrm{V}}(\mathbf{h}) = \frac{2\sum_m \xi_m \bar{r}_{m1}\bar{r}_{m2}\bar{R}_{m3}^4(1+c_m)^6 n_{\mathbf{h}}^{-1}\sum_k \tau_{km}}{\sum_m \xi_m \bar{r}_{m1}\bar{r}_{m2}\bar{R}_{m3}^3(1+c_m)^3}, \quad (28)$$

$$\sigma_{km}^{-1} = \big(h_{km1}^2/\bar{r}_{m1}^2 + h_{km2}^2/\bar{r}_{m2}^2\big)^{1/2},$$

$$\tau_{km} = 1/|h_{km3}| \quad \text{if } \sigma_{km}^{-1} = 0,$$

$$\tau_{km} = 1/|h_{km3}| - (4/\pi)\sigma_{km}\big[-(2/3) + (2/3)(1-q_{km}^2)^{1/2}$$
$$+ (1/3)q_{km}^2(1-q_{km}^2)^{1/2} + q_{km}\arcsin q_{km}\big] + (1/\pi)\sigma_{km}^2|h_{km3}|$$
$$\times \big[(1/2)q_{km}(1-q_{km}^2)^{1/2} - (1/2)\arcsin q_{km}$$
$$+ q_{km}^3(1-q_{km}^2)^{1/2} + 2q_{km}^2\arcsin q_{km}\big] \quad \text{if } 0 < \sigma_{km}^{-1} < |h_{km3}|,$$

$$q_{km} = \sigma_{km}^{-1}/|h_{km3}|,$$

$$\tau_{km} = (8/3\pi)\sigma_{km} - (1/4)\sigma_{km}^2|h_{km3}| \quad \text{if } \sigma_{km}^{-1} \ge |h_{km3}|.$$

4.4. Crystallite morphology and size distribution in zinc oxide

The shapes and sizes of crystallites determined by X-ray diffraction on a sample of zinc oxide prepared by a method

---

[7] The need for a multimodal distribution will be explained below.

Table 4
The refined principal diameters (Å), relative dispersions, weight parameter and reliability factors for the simplest 'physical' model using bimodal ellipsoidal crystallite shape and lognormal size distribution; $\bar{\omega}_m = \bar{\chi}_m = \bar{\varphi}_m = 0$ for both modes.

Mode 1	Mode 2
$\bar{D}_{11} = 24.4\,(22)$	$\bar{D}_{21} = 207\,(20)$
$\bar{D}_{12} = 102\,(9)$	$\bar{D}_{22} = \bar{D}_{21}$
$\bar{D}_{13} = 181\,(15)$	$\bar{D}_{23} = 62.2\,(34)$
$c_1 = 0.94\,(8)$	$c_2 = 0$
$\xi_1 = 0.54\,(5)$	
$R_{\mathrm{p}} = 6.26\%$	$R_{\mathrm{wp}} = 10.49\%$

Table 5
The refined principal diameters (Å), relative dispersions, weight parameter and reliability factors for the simplest 'physical' model using bimodal elliptical cylinder crystallite shape and lognormal size distribution; $\bar{\omega}_m = \bar{\chi}_m = \bar{\varphi}_m = 0$ for both modes.

Mode 1	Mode 2
$\bar{D}_{11} = 29.0\,(25)$	$\bar{D}_{21} = 161\,(16)$
$\bar{D}_{12} = 120\,(10)$	$\bar{D}_{22} = \bar{D}_{21}$
$\bar{D}_{13} = 165\,(13)$	$\bar{D}_{23} = 53.5\,(24)$
$c_1 = 0.76(6)$	$c_2 = 0$
$\xi_1 = 0.44\,(6)$	
$R_{\mathrm{p}} = 5.59\%$	$R_{\mathrm{wp}} = 11.16\%$

similar to those described in §3.1 were reported many years ago by Louër *et al.* (1983). In that sample identical apparent sizes for the peaks (100) and (110) were observed, and the crystallites were considered cylindrical on average with the cylinder axis along the sixfold axis. The transmission electron micrograph showed prismatic crystallites with the cross sections normal to the sixfold axes of regular or irregular hexagons. Therefore, the shape of the crystallites is variable but the sixfold axis is always the prism axis. We consider this property to also apply to the present sample. The present sample was synthesized under different conditions and cylindrical symmetry of the apparent crystallites is missing. Indeed, we can observe in Table 3 that the averaged column lengths D_{V} and D_{A} for the peaks (100) and (110) are significantly different. Consequently the shape of the crystallites cannot be approximated by circular cylinders but rather by elliptical cylinders or by ellipsoids; we can then use the models developed in §4.3. As *a priori* information we presume that the principal axis $\mathbf{p}_3$ is parallel to the sixfold axis $\mathbf{c}$. In this case the Euler angle χ is zero, and consequently φ becomes additive to ω and can be taken as zero. The angle ω must have a small value, if it is not zero. This can be understood by inspecting the equatorial cross sections of the apparent crystallites from Fig. 5(*a*). The contours in this figure are approximately hexagons with rounded corners and curved concave edges. If ω is zero, such contours can be obtained by superposition of identical ellipses rotated with respect to one another by 60°. For large values of ω a splitting of the hexagon corners should be observed, because both $\mathbf{a}$ and $\mathbf{b}^*$ are twofold axes. Certainly the splitting cannot be seen if ω is small. Finally, though both ellipsoid and elliptical cylinder have convex shapes, concave segments can also be observed in the contours in the vertical cross sections in Fig. 5(*b*). If for the equatorial cross sections this peculiarity was easy to understand, for the vertical cross sections it can be explained only if the crystallite distribution [equation (22)] is bimodal.

The column length data from Table 3 were fitted by minimizing equation (16) with the two models developed in §4.3, taking into account the constraints discussed previously. Initially we took $\bar{\omega}_1 = \bar{\omega}_2 = 0$ with nine parameters remaining free: $\bar{r}_{m1}$, $\bar{r}_{m2}$, $\bar{R}_{m3}$, c_m ($m = 1, 2$) and ξ_1. The refinement resulted in very similar ratios $\bar{r}_{21}$ and $\bar{r}_{22}$ and a very small value for c_2, with much larger standard uncertainty. The fit was repeated setting $\bar{r}_{22} = \bar{r}_{21}$ and $c_2 = 0$. Finally, a third fit was

performed with the parameter $\bar{\omega}_1$ free. As expected, its refined value was small with larger standard uncertainty and with practically no change in the other parameters, so we returned to the second fit. The results of the fits for ellipsoids and elliptical cylinders are given in Tables 4 and 5, respectively. In these tables we report the principal diameters in place of the principal radii and their ratios. The corresponding cross sections through the apparent crystallites are compared in Figs. 6 and 7, respectively, with those obtained by whole
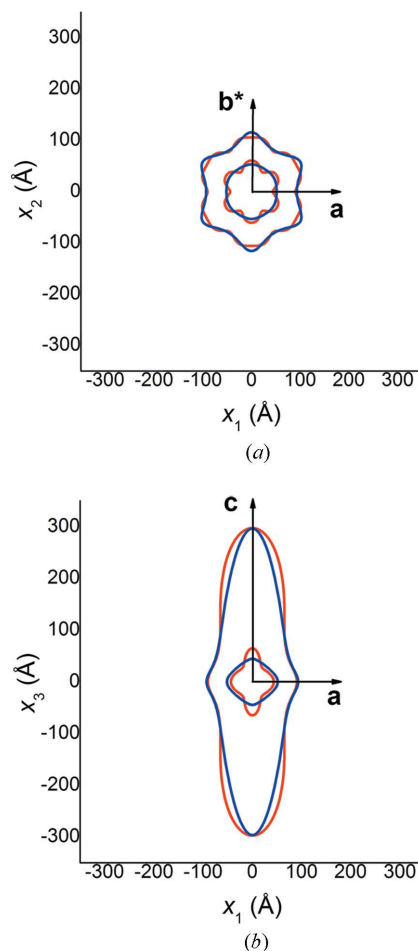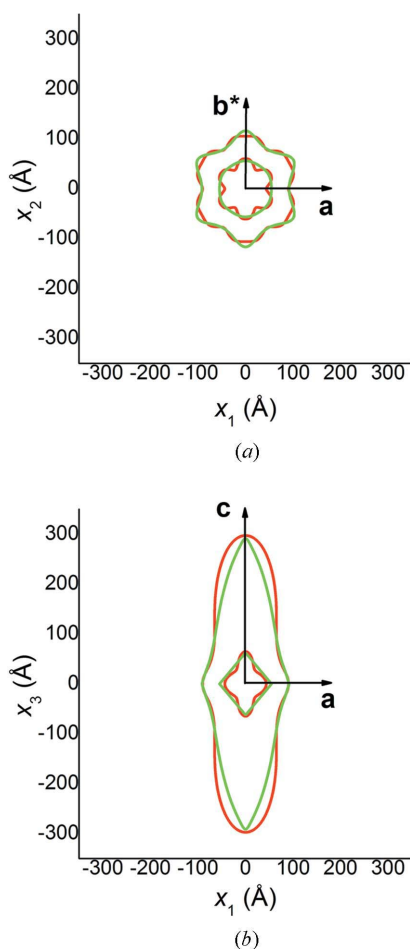

(*a*)

(*b*)

Figure 6
Equatorial (*a*) and vertical (*b*) cross sections through the apparent crystallites. Blue contours: ellipsoidal model; red contours: spherical harmonics model.

Table 6
The refined Euler angles $\bar{\chi}_m$ and $\bar{\varphi}_m$, principal diameters (Å), relative dispersions, weight parameter and reliability factors for the 'physical' model using bimodal ellipsoidal crystallite shape and lognormal size distribution; $\bar{\omega}_m = 0$ for both modes.

Mode 1	Mode 2
$\bar{\chi}_1 = 18.5\,(8)$	$\bar{\chi}_2 = \bar{\chi}_1$
$\bar{\varphi}_1 = 10.0\,(2)$	$\bar{\varphi}_2 = \bar{\varphi}_1$
$\bar{D}_{11} = 53\,(6)$	$\bar{D}_{21} = 509\,(133)$
$\bar{D}_{12} = 804\,(240)$	$\bar{D}_{22} = \bar{D}_{21}$
$\bar{D}_{13} = 497\,(50)$	$\bar{D}_{23} = 41.4\,(36)$
$c_1 = 0.33\,(6)$	$c_2 = 0$
$\xi_1 = 0.35\,(8)$	
$R_\mathrm{p} = 6.19\%$	$R_\mathrm{wp} = 10.15\%$

pattern fitting using the phenomenological model with spherical harmonics. The fit is imperfect and some details are smoothed, mostly for the area-averaged apparent crystallite. This should be expected if we take into account the idealized and simplified character of the crystallite shape models. Nevertheless, this is an approximate representation of the zinc oxide microstructure. It is notable that the refined parameters

Figure 7
Equatorial (*a*) and vertical (*b*) cross sections through the apparent crystallites. Green contours: elliptical cylinders model; red contours: spherical harmonics model.

in Tables 4 and 5 have comparable values, the relative differences being around 20%. Consequently, we can imagine that both the ellipsoids and the elliptical cylinders approximate two types of strongly anisotropic crystallites that are present in the sample with approximately equal weights. The first mode represents thin plates parallel to the $\mathbf{b}^*\mathbf{c}$ plane and having a broad lognormal size distribution. These crystallites are responsible for the super-Lorentzian peak shapes in the diffraction pattern. The second mode represents short rods with axes along $\mathbf{c}$, having a very sharp size distribution. The existence of this mode explains the concave segments on the vertical cross section contours of the apparent crystallites. In analogy to the sample of zinc oxide reported by Louër *et al.* (1983), the plates and rods in the present sample could, in fact, be prisms whose cross sections normal to the *c* axis are irregular and regular hexagons, respectively. Unfortunately, for the present sample, TEM data confirming these crystallite morphologies and size distributions are not available owing to the difficulty of dispersing the crystallites agglomerated in pseudomorphic particles obtained from topotactic decomposition reactions.

4.5. *A priori* information and the stability of the solution

To find the solutions reported in the previous section we used the *a priori* information that one principal axis of the ellipsoids or elliptical cylinders approximating the crystallite shapes is parallel to the sixfold axis. Let us see what happens if we ignore this information and include the Euler angles in the list of the fitting parameters. For the ellipsoidal shape we performed several minimizations changing the starting values of the Euler angles. For simplicity these angles were constrained to be the same for both modes. The starting values for the remaining parameters were those from Table 4. When the initial values of the Euler angles are small, their refined values remain small but with high standard uncertainties, and thus are not significant. All other refined parameters and R factors remain practically unchanged. The solution from Table 4 is reproduced except for larger values of standard uncertainties. By contrast, if the minimization begins with high values of the Euler angles, only one of them becomes not significant, $\bar{\omega}_m$ or $\bar{\varphi}_m$, and the rest of the parameters become significantly different from those in Table 4. The result of the fit with $\bar{\omega}_m$ fixed to zero and $\bar{\chi}_m$ and $\bar{\varphi}_m$ free is given in Table 6. At first sight, if we take into account only the reliability factors, this fit is slightly better than those from Table 4, but in fact it represents a false solution. Indeed, if we calculate the maximum anisotropy as the ratio between the greatest and the smallest crystallite average diameters, for the data in Table 4 this quantity is 7.4 (9) for mode 1 and 3.3 (4) for mode 2, but for the data in Table 6 these numbers are 15 (5) and 12 (3), respectively. The last two numbers are excessively large with large standard uncertainties. We can say that the solution from Table 6 is not smoothed[8] relative to those from Table 4. As can

---

[8] The terms 'smoothed solution' and 'stabilized solution' are frequently met in the literature when ill-posed inverse problems like deconvolution are discussed.
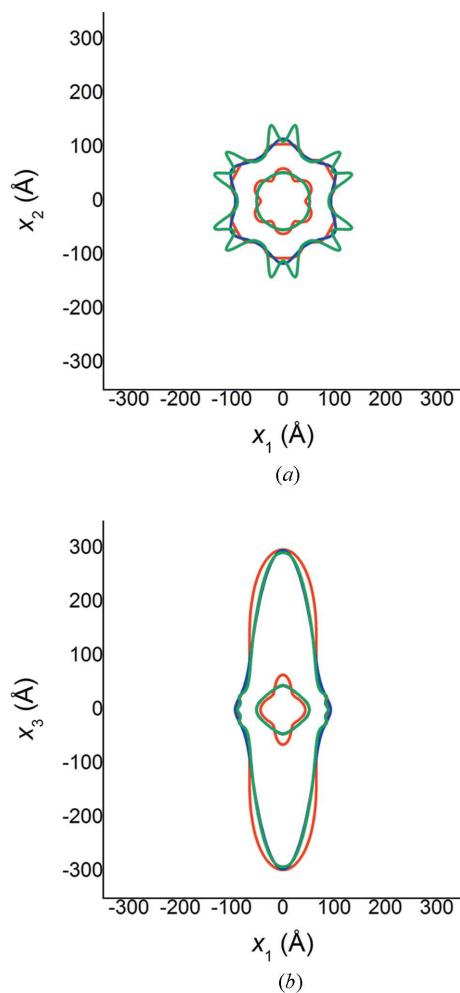
Figure 8
Equatorial (*a*) and vertical (*b*) cross sections through the apparent crystallites. Red: spherical harmonics model; blue: ellipsoidal model with Euler angles fixed according to the *a priori* information; green: ellipsoidal model with Euler angles $\bar{\chi}_m$ and $\bar{\varphi}_m$ refined.

be seen in Fig. 8, the non-smoothed character is also reflected in the volume-averaged apparent crystallite reconstructed with this solution. This is manifested in both the equatorial and the vertical cross sections as ripples in the vicinity of the equatorial plane. A similar but different solution can be obtained if $\bar{\varphi}_m$ is fixed to zero and $\bar{\omega}_m$ and $\bar{\chi}_m$ are refined. We can conclude that if the *a priori* information is ignored the solution becomes unstable, obtaining very probably an incorrect description of the morphologies and the distribution of the crystallites. At least for this sample, the pattern does not contain enough information to refine univocally the crystallite orientations together with other anisotropic size distribution parameters. Would such refinement be possible if the distribution had only one mode, that is, a smaller number of parameters? This question is still open.

5. Conclusions

A new improved spherical harmonics model to describe the size anisotropy in whole powder pattern fitting was achieved

by combining the previously published model (Popa, 1998) with the peak profile for spherical crystallites and a lognormal size distribution. Like the old model, the improved model is phenomenological and is appropriate for implementation in existing Rietveld codes. The new method is able to fit difficult patterns where conventional profiles fail and to estimate both volume- and area-averaged apparent crystallites.

In principle, the apparent crystallites determined in this way (or by conventional methods if available) can be further used in a least-squares refinement program to fit the parameters of a physical model: the shape, orientation and size distributions of crystallites. The diffraction pattern may not have enough information to sustain too complex a model; in order to achieve stable solutions, it is then advisable to use simple models and to take advantage of some *a priori* information, which would decrease the number of fitting parameters. On the other hand, we must be aware that, because the models of crystallite morphology and distribution have an idealized character, one expects only an approximate quantitative reproduction of the apparent crystallites. Moreover, even if a stable solution is achieved in the context of a given model, it does not mean that this solution is unique, as several models may fit the data equally well. To confirm or reject a possible model, additional information, such as that obtained by TEM, is necessary. This is valid not only for the size-broadening effect but also for the strain-broadening effect. We think that, in principle, the diffraction alone can unambiguously determine with a good accuracy only an apparent microstructure.

APPENDIX A
Analytical approximation of $\bar{\Phi}$ for lognormal distribution of spherical crystallites

[From Popa & Balzar (2002).] The exact expression of $\bar{\Phi}(x; c)$ for the lognormal distribution is

$$\bar{\Phi}(x; c) = \pi^{-1/2} \int_{-\infty}^{\infty} dt \exp(-t^2) \Phi\left(x(1+c)^{7/2}\right.$$
$$\left. \times \exp\{t[2\ln(1+c)]^{1/2}\}\right). \tag{29}$$

Here $\Phi(x)$ is the interference function for a sphere:

$$\Phi(x) = (x^2 + \sin^2 x - x \sin 2x)/x^4.$$

The integral in equation (29) can be performed by a Gauss–Hermite quadrature requiring a large number of nodes to reach a given accuracy. For implementation in existing whole pattern fitting codes (Rietveld included) an appropriate analytical approximation is available:

$$\bar{\Phi}(x; c) \simeq$$

$$(8/3)(1+c)^{-3}\left[\eta_1\alpha_1^{-1}(1+4x^2/\alpha_1^2)^{-1} + \eta_2\alpha_2^{-1}(1+4x^2/\alpha_2^2)^{-1}\right.$$
$$\left. + \eta_3\alpha_3^{-1}\begin{cases} \exp(-4x^2/\pi\alpha_3^2) & \text{if } 0 \leq c \leq 1 \\ (1+4x^2/\alpha_3^2)^{-1} & \text{if } 1 < c \leq 6 \end{cases}\right]. \tag{30}$$

In (30) the parameters η_1, α_1, η_2 and α_2 are independent empirical functions of c, but η_3 and α_3 are constrained to have $\bar{\Phi}(0; c) = 1$. These are the following (always $0 \leq \eta_i \leq 1$):

$$\eta_1(c) = 0.25631 + 0.018638\,c + 0.001155\,c^2 \\ + 3.5671\,c\,\exp(-2.0467\,c^{0.93346}),$$

$$\alpha_1(c) = 4.02326\,\exp(-44.6429\,c) + 3.13982\,\exp(-7.01128\,c) \\ + 0.580742\,\exp(-0.413958\,c) + 0.381245\,\exp(-1.10827\,c),$$

$$\eta_2(c) = \begin{cases} 0 & \text{if } 0 \leq c \leq 0.4 \\ 0.59951 - 0.020058\,(c - 0.4) \\ \quad - 0.45347/[1 + 3.3933\,(c - 0.4)^2] \\ \quad - 0.14604\,\exp[-0.49272\,(c - 0.4)^2] & \text{if } 0.4 \leq c \leq 6, \end{cases}$$

$$\alpha_2(c) = 0.32781 \, / \, \big[1 + 1.5399\,(c - 0.4) - 0.21223\,(c - 0.4)^2 \\ + 0.18158\,(c - 0.4)^3\big],$$

$$\eta_3 = 1 - \eta_1 - \eta_2, \quad \alpha_3 = \eta_3 \, / \, \big[3(1 + c)^3/8 - \eta_1/\alpha_1 - \eta_2/\alpha_2\big].$$

References

Auffrédic, J. P. & Louër, D. (1987). *React. Solids*, **4**, 105–115.

Bertaut, E. F. (1949). *C. R. Acad. Sci.* **228**, 492–494.

Casas-Cabanas, M., Palacin, M. R. & Rodriguez-Carvajal, J. (2005). *Powder Diffr.* **20**, 334–344.

Greaves, C. (1985). *J. Appl. Cryst.* **18**, 48–50.

Krill, C. E. & Birringer, R. (1998). *Philos. Mag. A*, **77**, 621–640.

Langford, J. I., Boultif, A., Auffrédic, J. P. & Louër, D. (1993). *J. Appl. Cryst.* **26**, 22–33.

Langford, J. I. & Louër, D. (1982). *J. Appl. Cryst.* **15**, 20–26.

Langford, J. I., Louër, D. & Scardi, P. (2000). *J. Appl. Cryst.* **33**, 964–974.

Larson, A. C. & Von Dreele, R. B. (1986). *General Structure Analysis System (GSAS)*. Report LAUR 86-748. Los Alamos National Laboratory, New Mexico, USA.

Leoni, M. & Scardi, P. (2004). *J. Appl. Cryst.* **37**, 629–634.

Louër, D., Auffrédic, J. P., Langford, J. I., Ciosmak, D. & Niepce, J. C. (1983). *J. Appl. Cryst.* **16**, 183–191.

Louër, D. & Langford, J. I. (1988). *J. Appl. Cryst.* **21**, 430–437.

Louër, D., Weigel, D. & Langford, J. I. (1972). *J. Appl. Cryst.* **5**, 353–359.

Lutterotti, L. (1997). *Material Analysis Using Diffraction (MAUD)*. http://www.Ing.unitn.it/~maud/.

Lutterotti, L., Matthies, S. & Wenk, H. R. (1999). *Commission on Powder Diffraction Newsletter*, No. 21, pp. 14–15, http://www.iucr.org/iucr-top/comm/cpd/html/newsletter21.html.

Pawley, G. S. (1981). *J. Appl. Cryst.* **14**, 357–361.

Popa, N. C. (1992). *J. Appl. Cryst.* **25**, 611–616.

Popa, N. C. (1998). *J. Appl. Cryst.* **31**, 176–180.

Popa, N. C. & Balzar, D. (2001). *J. Appl. Cryst.* **34**, 187–195.

Popa, N. C. & Balzar, D. (2002). *J. Appl. Cryst.* **35**, 338–346.

Rodriguez-Carvajal, J. (2001). *Commission on Powder Diffraction Newsletter*, **26**, 12–19, http://www.iucr.org/iucr-top/comm/cpd/html/newsletter26.html.

Scardi, P. & Leoni, M. (2002). *Acta Cryst.* A**58**, 190–200.

Scardi, P. & Leoni, M. (2006). *J. Appl. Cryst.* **39**, 24–31.

Scherrer, P. (1918). *Nachr. Gött.* **2**, 98–100.

Thompson, P., Cox, D. E. & Hastings, J. B. (1987). *J. Appl. Cryst.* **20**, 79–83.

Ungár, T., Gubicza, J., Ribárik, G. & Borbély, A. (2001). *J. Appl. Cryst.* **34**, 298–310.

Vargas, R., Louër, D. & Langford, J. I. (1983). *J. Appl. Cryst.* **16**, 512–518.

Warren, B. E. & Averbach, B. L. (1950). *J. Appl. Phys.* **21**, 595–599.

Warren, B. E. & Averbach, B. L. (1952). *J. Appl. Phys.* **23**, 497.

Wilson, A. J. C. (1962). *Nature (London)*, **193**, 568–569.

Wilson, A. J. C. (1969). *J. Appl. Cryst.* **2**, 181–183.

Young, R. A. & Sakthivel, A. (1988). *J. Appl. Cryst.* **21**, 416–425.